Direct Imaging of Resonant Phonon-Magnon Coupling

Chenbo Zhao, Zhizhi Zhang, Yi Li, Wei Zhang, John E. Pearson, Ralu Divan, Qingfang Liu, Valentine Novosad, Jianbo Wang, and Axel Hoffmann

Phys. Rev. Applied **15**, 014052 — Published 27 January 2021

DOI: 10.1103/PhysRevApplied.15.014052

Direct Imaging of Resonant Phonon-Magnon Coupling

Chenbo Zhao[1,2], Zhizhi Zhang[1], Yi Li[1], Wei Zhang[3,1], John E. Pearson[1], Ralu Divan[4],
Qingfang Liu[2], Valentine Novosad[1], Jianbo Wang[2†], and Axel Hoffmann[1,5‡a]
[1] Materials Science Division, Argonne National Laboratory, Argonne, Illinois 60439, USA
[2] Key Laboratory of Magnetism and Magnetic Materials of the Ministry of Education,
Lanzhou University, Lanzhou 730000, People's Republic of China
[3] Department of Physics, Oakland University, Rochester, MI 48309, USA
[4] Center for Nanoscale Materials, Argonne National Laboratory, Argonne, IL 60439, USA
[5] Department of Materials Science and Engineering, University of Illinois at Urbana-Champaign, Urbana, IL 61801, USA

ABSTRACT

Detection of phonons is critical for the research on the interconversion between resonantly coupled magnons and phonons. Here we report the direct visualization of the resonant coupling of magnons and phonons by micro-focused Brillouin light scattering on the Ni/LiNbO$_3$ hybrid heterostructure. The static patterns of surface acoustic wave phonons, originating from the interference between the incident wave $\psi_0(A_0, \boldsymbol{k}, \varphi_0)$ and reflected wave $\psi_1(A_1, -\boldsymbol{k}, \varphi_1)$, can be modulated by magnetic field due to the magnon-phonon coupling. By analyzing the information of phonons obtained from Brillouin spectroscopy, the properties of the magnon system (Ni film), e.g., ferromagnetic resonance field and resonance linewidth can be determined. The results provide spatially resolved information about phonon manipulation and detection in a coupled magnon-phonon system.

---

[a] †wangjb@lzu.edu.cn
‡axelh@illinois.edu

INTRODUCTION

Spin waves and their quasiparticles, i.e., magnons, are promising for high frequency information processing and transmission [1-6], as well as logic devices [1,7,8]. However, the efficient generation of spin waves with long propagation distances, remains a challenge due to magnetic losses in metallic ferromagnets [9,10]. At the same time, surface acoustic wave (SAW) phonons have the advantage of short wavelength and long propagating distances of several millimeters, e.g., in $LiNbO_3$ crystals [11]. Coupling magnons to SAW phonons can avoid the rapid decay of spin waves, and thus provides a new opportunity for information interconversion of phononic and spin degrees of freedom [12-22]. More recently, SAW induced off-resonant magneto-acoustic waves with different wavelengths and long propagation distances have been imaged directly by using x-ray magnetic circular dichroism [23]. The wave vector and amplitude of the off-resonant magneto-acoustic wave can be modulated by SAW and magnetic field, respectively. Nevertheless, the question remains how the phonon transport can be modulated by magnons.

The resonant magnon-phonon coupling can be probed based on magnetic field dependent microwave transmission measurements [20-22,24,25] and time-resolved magneto-optical detection of magnetization dynamics [26]. However, the existing methods cannot provide direct information and spatial mapping of the phonon evolution modulated by magnons. Conversely, optical detection of hypersonic SAW phonons has been realized in bulk transparent materials [11,27-30] using Brillouin light scattering (BLS). More recently, the spatially resolved patterns of SAW phonons were observed directly by using BLS [31]. This provides an opportunity to apply Brillouin light scattering spectroscopy for obtaining direct information on both the magnon and phonon aspects of resonant magnon-phonon coupling.

In the present work, we focus on directly visualizing the resonant coupling of magnons and phonons using an optical approach. The interference patterns of multiple SAWs carrying spin information were detected using micro focused Brillouin light scattering (μ-BLS) on Ni/$LiNbO_3$ hybrid heterostructures. The BLS intensity has been found to be minimum at the ferromagnetic resonance (FMR) field of Ni, where SAW phonons are strongly attenuated by magnons, while the contrast of the interference patterns remains clearly visible, which provides a directly visualization of the magnetic field modulation of SAW phonons by resonant coupling of magnon-phonon. By fitting a detailed theoretical model [32-34] to the magnetic field dependence of the spatial-averaged and frequency-averaged BLS signal intensities, the estimated value of the FMR field and resonance linewidth is consistent with that obtained based on SAW magnetic field dependent microwave-transmission measurements. The results provide the opportunities for exploring phonon manipulation and detection in the presence of magnetization dynamics.

RESULTS AND DISCUSSION

Figure 1(a) shows an optical image of the Ni/LiNbO$_3$ hybrid device with a 50-nm thick rectangular Ni film. In these devices, the finger width and spacing of the interdigitated transducer (IDT) fabricated with 50-nm thick Al are both 3 μm (resulting in a fundamental SAW wavelength $\lambda_0 = 12$ μm) on a 127.86° Y-X cut LiNbO$_3$ substrate with a thickness of 500 μm. By connecting a microwave source to the left IDT we excite SAW $\psi_0(A_0, \boldsymbol{k}, \varphi_0)$ at 3.56 GHz, which corresponds to the 11th harmonic, where A_0 is amplitude, $\boldsymbol{k}$ is the wave vector, and φ_0 is the phase of SAW. As was shown previously [28,35,36], a high-quality reflector for a SAW can be made using an array of shorted or open interdigital electrodes. In our device, the right unconnected IDT (open interdigital electrodes) acts as a reflector and generates a counter-propagating wave $\psi_1(A_1, -\boldsymbol{k}, \varphi_1)$. The waves ψ_0 and ψ_1 share the same frequency f and have a fixed phase difference ($\Delta\varphi = \varphi_0 - \varphi_1$), but different amplitude. These two waves are expected to produce acoustic fields with a time-independent spatial variation via interference. The SAW generates a concomitant internal rf magnetic field originating from magnetoelastic coupling between the SAW elastic strain field and the Ni film. This dynamic effective magnetic field drives subsequently FMR in the Ni film for specific DC magnetic fields H. In order to achieve resonant magnon-phonon coupling, the DC magnetic field H is applied in a direction with an angle $\theta = 30^{\circ}$ with respect to the SAW wavevector k_{SAW} of ψ_0.

Our BLS spectrometer is based on continuous wave solid state laser with $\lambda = 532$ nm, which is focused down to 250 nm. The inelastic backscattering by quasiparticles, i.e., phonons or magnons, results in frequency-shifted photons that are collected by photodetector after passing through a frequency selective Tandem Fabry-Pérot interferometer (TFPI). This allows to directly detect the frequency of the magnons or phonons with high spatial resolution by scanning the sample with respect to the focused incident laser beam. First, the laser spot was located on one of the IDT fingers, and the corresponding BLS signal is shown in Fig. 1(b). The BLS signal is independent of H near 3.56 GHz, which indicates that SAW phonons are excited and detected, where the Al film acts as a mirror [11,29,30] for SAW phonons detection using μ-BLS. Fig. 1(c) shows an optical image of the IDT fingers and the green rectangular region represents the area for the spatially resolved measurements. During the spatial measurement process, a high-resolution positioning system together with an active widefield imaging feedback [using optical images as shown in Fig. 1(c)] is used to position the sample with high stability relative to the laser focus. Thus, the intensity distribution of the phonons is measured by moving the sample and keeping the optics fixed. Fig. 1(d) shows the spatially resolved BLS intensity patterns over the measured region on one of the IDT fingers. The period of the spatial resolution patterns is estimated to be about 1 μm, which is consistent with the wavelength of 11th harmonic $\lambda_n = \lambda_0/n = 1.09$ μm, where $\lambda_0 = 12$ μm is the wavelength of the fundamental wave, and $n = 11$ is the harmonic order. The results indicate that these two waves, i.e., ψ_0 and ψ_1, produce acoustic fields with a static spatial variation via interference, and the lateral distribution of SAW phonons can be visualized directly using μ-BLS based imaging [11,27,29-31].

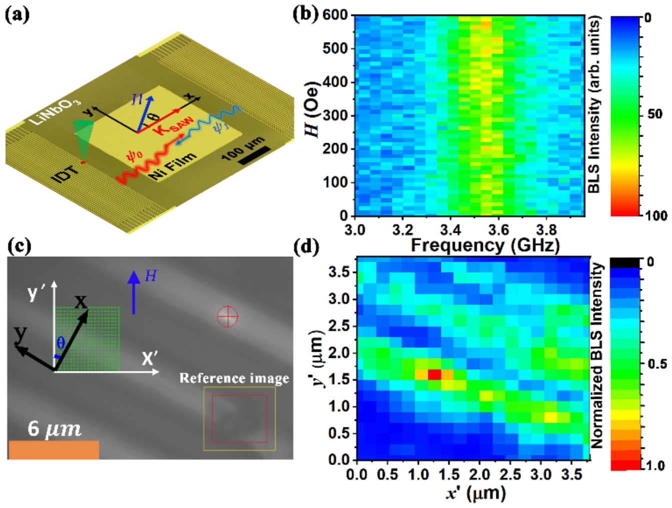

Figure 1: (a) Optical image of the Ni/LiNbO$_3$ hybrid device with a 50-nm thick Ni rectangular film. The green cone represents the BLS laser beam, and the red dot represents the position of

laser spot. SAW ψ_0 is excited using the left IDT, and the counter-propagating ψ_1 is generated via reflection from the right unconnected IDT. A DC magnetic field H is applied at an angle $\theta = 30^{\circ}$ with respect to the wavevector k_{SAW} of ψ_0. (b) Magnetic field H dependence of the BLS signal when the laser spot is located on one of the IDT fingers. (c) Optical image of the IDT fingers. The green rectangular region represents the area for the spatially resolved BLS measurements. The reference image is used for active stabilization of the position of the sample with respect to the laser focus. The magnetic field H and the wave vector k_{SAW} are along the y′ and x direction in the depicted coordinate systems, respectively. θ is fixed at $\theta = 30^{\circ}$. (d) Spatial resolved image of SAW phonons under a DC magnetic field $H = 600$ Oe.

Although the $LiNbO_3$ crystal is a perfect waveguide for SAW phonons propagation, it is difficult to directly detect the backscattering photons on the transparent substrate [27]. Figure 2(a) and (b) show the BLS intensity when the laser spot was located on the $LiNbO_3$ substrate and the Ni film, respectively. In order to exclude local variations, Figs. 2(a) and (b) are averaged results for several measurement points on the $LiNbO_3$ substrate and the Ni film, respectively. The BLS intensity on the $LiNbO_3$ is ten times weaker than it is on the Ni film at $H = 600$ Oe. According to a Gaussian fit to the frequency distribution of the SAW phonons as shown in Figs. 1(c) and (d), the line width of the SAW phonons (FWHM = 0.28 GHz) at 3.56 GHz is consistent with that obtained on the Ni film (FWHM = 0.23 GHz). However, the line width is larger than that (FWHM = 20 MHz) obtained by using from magneto-transmission measurements by using a vector network analyzer [34], and the main reason is the limited resolution of the interferometer of 100 MHz. The results of Figs. 1 and 2 indicate that the Ni film also can be used as a mirror to detected SAW phonons on the transparent substrate [11,29,30]. Notably, the H dependence of the BLS signal exhibits a gap near the FMR field of Ni [Fig. 2(b)]. The result is similar to our previous work based on magnetic field dependent microwave-transmission measurements by using vector network analyzer [34], where the transmission power exhibits a gap near the FMR field for the 5th, 7th and 11th harmonics of SAWs. The gap suggests that phonon-driven FMR occurs, and that the SAW phonons are strongly attenuated by magnons around the FMR field of the Ni film. To quantify the phonon absorption efficiency due to FMR, the H dependence of the frequency-averaged (3.15 GHz - 3.96 GHz) BLS intensity is plotted in Fig. 2(f). The obvious attenuation can be seen near $H = 200$ Oe. The SAW phonons absorption efficiency due to resonant coupling can be estimated as 26.5 %. As a reference, the frequency-averaged BLS signal on $LiNbO_3$ is shown in Fig. 2(e), which shows no dependence on H.

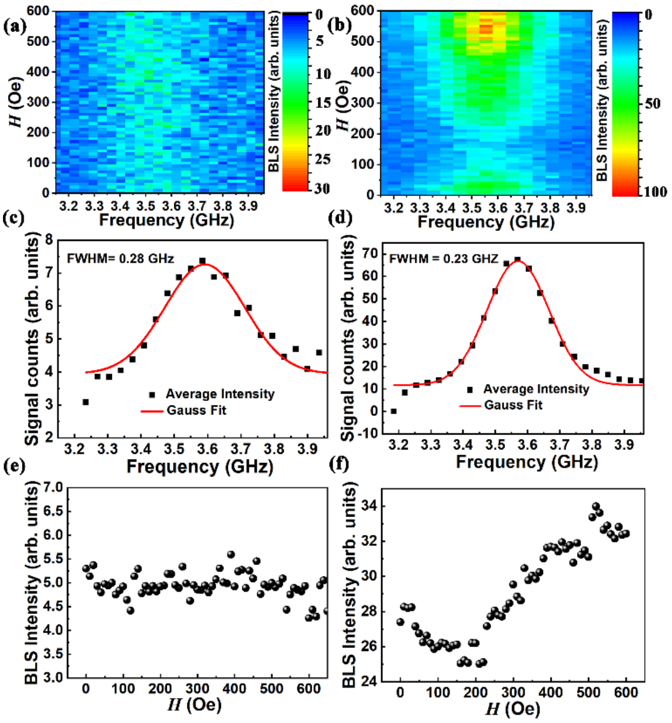

Figure 2: Magnetic field H dependence of the BLS intensity when the laser spot is located (a) on the $LiNbO_3$ substrate and (b) on the Ni film, respectively; (c) and (d) Frequency distribution for (a) and (b), respectively; (e) and (f) Magnetic field H dependence of the averaged BLS intensity for (a) and (b), respectively. The magnetic field H and wave vector k_{SAW} are along y′ and x direction in the coordinate system, respectively, and θ is fixed at $\theta = 30^{\circ}$, as shown in Fig. 1(a).

The BLS microscope has the advantage of being able to directly spatially image the SAW phonons and their modulation via FMR. The magnetic field H evolution of the SAW phonon interference patterns are shown in Figs. 3(a-i). As shown in Fig. 3(a) the magnetic field H and wave vector k_{SAW} are along the y′ and x directions of the depicted coordinate systems, respectively. θ is fixed at $\theta = 30^{\circ}$. The period of the stripe pattern is ~ 1 μm, which is consistent with the wavelength of the 11th harmonic SAW. The intensity of SAW phonon become weaker near FMR field [Fig. 3(e) and (f)] of the Ni film, which is direct evidence of the phonon absorption by resonant magnons. Conversely, the contrast remains clearly visible near the FMR field, which indicates the modulation of propagation phonons via resonant magnon-phonon coupling. In addition, the interference patterns become distorted below the saturation magnetic field [Fig. 3(h) and (i)], which can be attributed to the absorption of SAW phonons by hysteretic magnetization switching [20,37]. The results demonstrate how spatially resolved BLS imaging can directly image the resonant coupling of the SAW phonons and magnons.

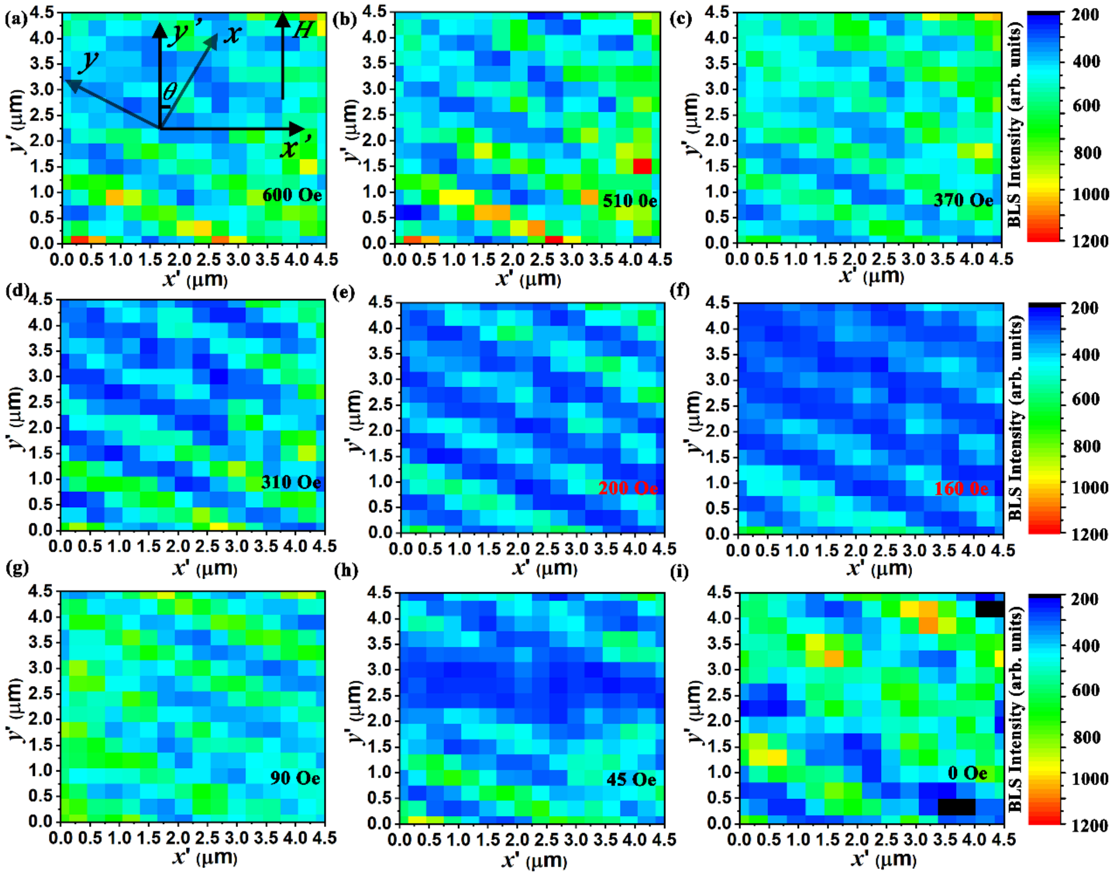

Figure 3: Magnetic field H evolution of the BLS spatially resolved images when the laser spot is located on the Ni film: (a) 600 Oe; (b) 510 Oe; (c) 370 Oe; (d) 310 Oe; (e) 200 Oe; (f) 160 Oe; (g) 90 Oe; (h) 45 Oe; (i) 0 Oe. The magnetic field H and wave vector k_{SAW} are along the y′ and x directions in the depicted coordinate systems, respectively. θ is fixed at $\theta = 30^{\circ}$.

As mentioned above, the waves, incident SAW $\psi_0(A_0, \boldsymbol{k}, \varphi_0)$ and reflected counter-propagating SAW $\psi_1(A_1, -\boldsymbol{k}, \varphi_1)$, have a fixed phase difference $\Delta\varphi$ and the same frequency f, but different amplitude. We can assume that the time-independent periodic patterns come from the interference of ψ_0 and ψ_1. The maximum strength $I_{\max}$ and minimum strength $I_{\min}$ of the interference patterns can be written as: $I_{\max} = {A_0}^2 + {A_1}^2 + 2A_0A_1\cos(\Delta\varphi)$ and $I_{\min} = {A_0}^2 + {A_1}^2 - 2A_0A_1\cos(\Delta\varphi)$, respectively. In order to analyze the interference patterns of the SAWs, the spatially resolved BLS intensity along the x′direction (y'= 1.5 μm) at different H are plotted and fitted using a sinusoidal function:

$$I = I_0 + A\sin\frac{2\pi(x'-x'_c)}{\lambda'}, \quad (1)$$

where λ' is the period, and I_0 and x'_c are constants, respectively. In Fig. 4(a) the spatially resolved BLS intensity [Fig 3(e)] along the x ′direction (y'= 1.5 μm) at H = 200 Oe is plotted together with a fit to Eq. (1). According to the angle between the stripe pattern and the wave vector direction [x direction in Fig. 3(a)], the SAW wavelength λ_{SAW} and fitted λ' can be evaluated as: $\lambda_{\mathrm{SAW}}= \lambda'\sin\theta$. Using this relationship, $\lambda_{\mathrm{SAW}} = \lambda_0/\mathrm{n} = 1.09\ \mu\mathrm{m} = (\lambda'\sin 30° \mp 0.03)\ \mu\mathrm{m}$ is obtained from the fitting results, where $\lambda_0 = 12\ \mu\mathrm{m}$ is the wavelength of fundamental wave, and n = 11 is the harmonic order. In the case of other fields H in Fig. 3, the result of $\lambda_{\mathrm{SAW}}= (1 \mp 0.03)$ μm can also been determined. Therefore, the patterns come from the interference between the incident wave $\psi_0(A_0, \boldsymbol{k}, \varphi_0)$ and the reflected wave $\psi_1(A_1, -\boldsymbol{k}, \varphi_1)$. The minimum and maximum of BLS intensity of the interference patterns in Fig. 3 are proportional to $I_{\max}$ and $I_{\min}$, respectively. According to the fitting results, the values of $I_{\max}$ and $I_{\min}$ at different H can be obtained and the ratio of $I_{\max}/I_{\min}$ is constant for different H, as is shown in Fig. 4(b)

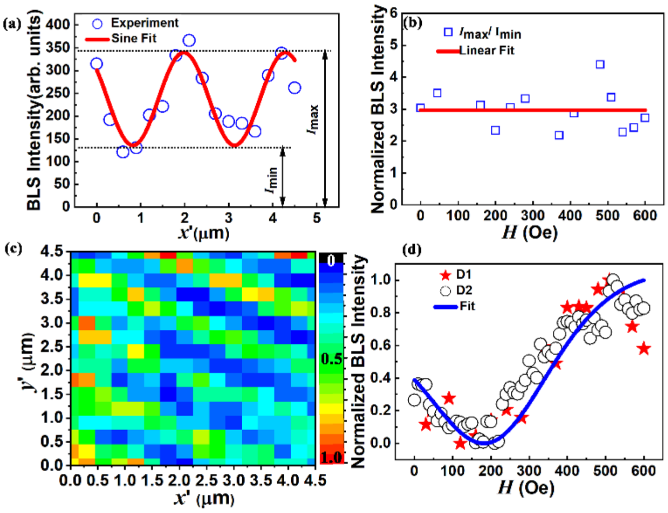

Figure 4: (a) BLS intensity evolution of [Fig 3(e)] at H = 200 Oe along the x’ direction and the solid line is a fit to Eq. (1). (b) H dependence of $I_{\max}/I_{\min}$ in Fig. 3, and the solid line is linear fit. (c) Averaged spatial resolution image at different H in Fig. 3. (d) Field H dependence of the normalized BLS intensity for the two measurements. The symbols are experimental data, and the solid line is a fit to theory using Eq. (2).

Since the H evolution for the interference patterns of the SAW were measured at the same region, the stripe patterns have the same phase. When all the stripe patterns at different magnetic field H are averaged, clear periodic patterns are obtained as shown in Fig. 4(c). This suggests that the patterns signal mainly come from SAW phonons. As discussion above, the *H* dependence of the BLS signal exhibits a gap near the FMR field of Ni [Fig 1 (b)], where the gap corresponds directly to the FMR field H_r and the resonance linewidth ΔH of Ni film. It is possible to fit the SAW phonon attenuation to *H* in order to estimate values of H_r and ΔH of Ni. Towards this end, the spatially-averaged BLS signal intensity of each pixel in the spatial patterns at different *H* [Fig. 3(a-i)] is calculated as data D1 [Stars in Fig 4(d)]. The magnetic field dependence of the frequency-averaged BLS intensity in Fig. 2(f) is normalized as data D2 [Circles in Fig. 4(d)]. The change of the SAW transmitted intensity (*I*) related to the phonon attenuation and generation during FMR can be rewritten as [32-34]:

$$I = I_0(1+p^2)^{-\frac{1}{2}}[1+(p+\beta)^2]^{-\frac{1}{2}} \exp\left[\frac{-\frac{\eta}{2}}{1+(p+\beta)^2}\right], \quad (2)$$

where, $p = (H - H_r)/\Delta H$, $\eta = C_1 f/\Delta H$, and $\beta = C_2 f^2/\Delta H$, H_r is the FMR field, resonance linewidth ΔH, f = 3.56 GHz is the frequency of the SAW, and *H* is the external magnetic field, and

$$C_1 = \frac{2\pi B_2^2 L}{C_{44} v_t M_s \mu_0} \quad (3)$$

$$C_2 = \frac{2A\rho(2\pi)^2}{C_{44} M_s \mu_0} \quad (4).$$

Where v_t = 3912 m/s is the Rayleigh acoustic wave velocity, $c = 3\times10^8$ m/s is the speed of light, $B_2 = 8.7\times10^6$ N/m^2 is the magnetoelastic parameter of Ni, $C_{44} = 1.22\times10^{11}$ N/m^2 is the elastic modulus of Ni, L = 12 µm is a characteristic length related to the SAW wavelength, $M_s = 4.7\times10^5$ A/m is the saturation magnetization, A is the exchange stiffness parameter, ρ = 8900 kg/m^3 is the density of Ni, and μ_0 is the magnetic permeability of vacuum. The data D1 and D2 can be fitted well using Eq. (2), as shown in Fig. 4(d). The fitted parameters of $\eta = 3.3$, $\beta = 0.04$ are consistent with the results of our previous results based on magnetic field dependent microwave-transmission measurements by using a vector network analyzer [34]. The obtained H_r and ΔH are (236 ∓ 30) Oe and (290 ∓ 36) Oe, respectively, which is consistent with the values ($H_r = 270$ Oe and $\Delta H = 290$ Oe) obtained from waveguide FMR experiments.

As shown here, the interference patterns of multiple SAW phonons coupled to magnon modes are well characterized using μ-BLS in the Ni/LiNbO$_3$ hybrid heterostructures. The Ni/LiNbO$_3$ hybrid heterostructures with resonant magnon-phonon coupling, can realize spatially complex transfers of energy between propagating spin and acoustic modes, thus creating a propagating magnetoelastic wave [15,23]. How to distinguish the spin signal and SAW signal from the BLS signal is an important issue for the future, e.g., the polarization analysis of the signal could be a powerful approach. Overall, our results open the directions for the application of SAW phonons in the fields of straintronics [16,18,20-22,24,25], sensing [38] and quantum information [39].

CONCLUSION

In conclusion, the interference patterns of multiple surface acoustic waves coupled to magnon modes were detected using micro-focused Brillouin light scattering in Ni/LiNbO$_3$ hybrid heterostructures. The intensity of SAW phonons become weaker near the FMR field of Ni, while the contrast of interference patterns remains clearly visible, which provides a direct image of the magnetic field modulation of surface acoustic wave phonons by resonant magnon-phonon coupling. By fitting the theory to the magnetic field dependence of the averaged Brillouin light scattering intensity, the ferromagnetic resonance field and resonance linewidth were estimated to be consistent with those obtained based on surface acoustic wave magnetic field dependent microwave-transmission measurements. The time-independent patterns can be attributed to the interference between the incident wave $\psi_0(A_0, \boldsymbol{k}, \varphi_0)$ and reflection wave $\psi_1(A_1, \boldsymbol{k}, \varphi_1)$. These results provide a direct spatially resolved characterization of phonon manipulation and detection in the presence of magnetization dynamics.

ACKNOWLEDGEMENTS

This work was performed at the Argonne National Laboratory and supported by the Department of Energy, Office of Science, Materials Science and Engineering Division. Use of the Center for Nanoscale Materials, an Office of Science user facility, was supported by the U.S. Department of Energy, Office of Science, Office of Basic Energy Sciences, under Contract No. DE-AC02-06CH11357. Chenbo Zhao acknowledges additional financial support from the China Scholarship Council (no. 201806180105) for a research stay at Argonne. The authors thank Vasyl Tyberkevych and Guozhi Chai for

useful discussion.

[1] A. V. Chumak, V. I. Vasyuchka, A. A. Serga, and B. Hillebrands, Magnon spintronics, Nature Physics **11**, 453 (2015).

[2] D. Grundler, Nanomagnonics around the corner, Nature Nanotechnology **11**, 407 (2016).

[3] Q. Wang, Pirro, P., Verba, R., Slavin, A., Hillebrands, B., A. V. Chumak, Reconfigurable nanoscale spin-wave directional coupler, Science advances **4**, e1701517 (2018).

[4] A. V. Sadovnikov, A. A. Grachev, E. N. Beginin, S. E. Sheshukova, Y. P. Sharaevskii, and S. A. Nikitov, Voltage-Controlled Spin-Wave Coupling in Adjacent Ferromagnetic-Ferroelectric Heterostructures, Physical Review Applied **7**, 014013 (2017).

[5] S. J. Hämäläinen, F. Brandl, K. J. A. Franke, D. Grundler, and S. van Dijken, Tunable Short-Wavelength Spin-Wave Emission and Confinement in Anisotropy-Modulated Multiferroic Heterostructures, Physical Review Applied **8**, 014020 (2017).

[6] Y. Li, W. Zhang, V. Tyberkevych, W. K. Kwok, A. Hoffmann, and V. Novosad, Hybrid magnonics: physics, circuits and applications for coherent information processing, Journal of Applied Physics **128**, 130902 (2020).

[7] K. Ganzhorn, S. Klingler, T. Wimmer, S. Geprägs, R. Gross, H. Huebl, and S. T. B. Goennenwein, Magnon-based logic in a multi-terminal YIG/Pt nanostructure, Applied Physics Letters **109**, 022405 (2016).

[8] B. Rana and Y. Otani, Voltage-Controlled Reconfigurable Spin-Wave Nanochannels and Logic Devices, Physicanl Review Applied **9**, 014033 (2018).

[9] A. Barra, A. Mal, G. Carman, and A. Sepulveda, Voltage induced mechanical/spin wave propagation over long distances, Applied Physics Letters **110**, 072401 (2017).

[10] V. E. Demidov, S. Urazhdin, R. Liu, B. Divinskiy, A. Telegin, and S. O. Demokritov, Excitation of coherent propagating spin waves by pure spin currents, Nature Communications **7**, 10446 (2016).

[11] B. Vincent, J. K. Krüger, O. Elmazria, L. Bouvot, J. Mainka, R. Sanctuary, D. Rouxel, and P. Alnot, Imaging of microwave-induced acoustic fields in $LiNbO_3$ by high-performance Brillouin microscopy, Journal of Physics D: Applied Physics **38**, 2026 (2005).

[12] M. Foerster, F. Macià, N. Statuto, S. Finizioet, A. Hernández-Mínguez, S. Lendínez, P. V. Santos, J. Fontcuberta, J. M. Hernàndez, M. Kläui, L. Aballe, Direct imaging of delayed magneto-dynamic modes induced by surface acoustic waves, Nature Communications **8**, 407 (2017).

[13] A. Kamra, H. Keshtgar, P. Yan, and G. E. W. Bauer, Coherent elastic excitation of spin waves, Physical Review B **91**, 104409 (2015).

[14] M. Montagnese, M. Otter, X. Zotos, D. A. Fishman, N. Hlubek, O. Mityashkin, C. Hess, R. S. Martin, S. Singh, A. Revcolevschi, P. H. M. van Loosdrecht, Phonon-Magnon Interaction in Low Dimensional Quantum Magnets Observed by Dynamic Heat Transport Measurements, Physical Review Letters **110**, 147206 (2013).

[15] P. Graczyk and M. Krawczyk, Coupled-mode theory for the interaction between acoustic waves and spin waves in magnonic-phononic crystals: Propagating magnetoelastic waves, Physical Review B **96**, 024407 (2017).

[16] R. Verba, I. Lisenkov, I. Krivorotov, V. Tiberkevich, and A. Slavin, Nonreciprocal Surface Acoustic Waves in Multilayers with Magnetoelastic and Interfacial Dzyaloshinskii-Moriya Interactions, Physical Review Applied **9**, 064014 (2018).

[17] I. S. Camara, J. Y. Duquesne, A. Lemaître, C. Gourdon, and L. Thevenard, Field-Free Magnetization Switching by an Acoustic Wave, Physical Review Applied **11**, 014045 (2019).

[18] M. Weiler, H. Huebl, F. S. Goerg, F. D. Czeschka, R. Gross, and S. T. Goennenwein, Spin

Pumping with Coherent Elastic Waves, Physical Review Letters **108**, 176601 (2012).

[19] C. L. Chang, R. R. Tamming, T. J. Broomhall, J. Janusonis, P. W. Fry, R. I. Tobey, and T. J. Hayward, Selective Excitation of Localized Spin-Wave Modes by Optically Pumped Surface Acoustic Waves, Physical Review Applied **10**, 034068 (2018).

[20] M. Weiler, L. Dreher, C. Heeg, H. Huebl, R. Gross, M. S. Brandt, and S. T. Goennenwein, Elastically Driven Ferromagnetic Resonance in Nickel Thin Films, Physical Review Letters **106**, 117601 (2011).

[21] M. Xu, J. Puebla, F. Auvray, B. Rana, K. Kondou, and Y. Otani, Inverse Edelstein effect induced by magnon-phonon coupling, Physical Review B **97**, 180301(R) (2018).

[22] L. Dreher, M. Weiler, M. Pernpeintner, H. Huebl, R. Gross, M. S. Brandt, and S. T. B. Goennenwein, Surface acoustic wave driven ferromagnetic resonance in nickel thin films: Theory and experiment, Physical Review B **86**, 134415 (2012).

[23] B. Casals, N. Statuto, M. Foerster, A. Hernandez-Minguez, R. Cichelero, P. Manshausen, A. Mandziak, L. Aballe, J. M. Hernandez, F. Macia, Generation and Imaging of Magnetoacoustic Waves over Millimeter Distances, Physical Review Letters **124**, 137202 (2020).

[24] R. Sasaki, Y. Nii, Y. Iguchi, and Y. Onose, Nonreciprocal propagation of surface acoustic wave in Ni/$LiNbO_3$, Physical Review B **95**, 020407(R) (2017).

[25] P. G. Gowtham, T. Moriyama, D. C. Ralph, and R. A. Buhrman, Traveling surface spin-wave resonance spectroscopy using surface acoustic waves, Journal of Applied Physics **118**, 233910 (2015).

[26] P. Kuszewski, J. Y. Duquesne, L. Becerra, A. Lemaître, S. Vincent, S. Majrab, F. Margaillan, C. Gourdon, and L. Thevenard, Optical Probing of Rayleigh Wave Driven Magnetoacoustic Resonance, Physical Review Applied **10**, 034036 (2018).

[27] R. J. Jiménez Riobóo, A. Sánchez-Sánchez, and C. Prieto, Optical find of hypersonic surface acoustic waves in bulk transparent materials, Physical Review B **94**, 014313 (2016).

[28] B. Vincent, T. Aubert, O. Seifaddini, O. Elmazria, D. Rouxel and J. K. Krüger, Brillouin spectroscopy applied to the characterization of SAW propagation losses in langasite, International Ultrasonics Symposium Proceedings, IEEE 539-542 (2010).

[29] S. Murata, T. Kawamoto, M. Matsukawa, T. Yanagitani, and N. Ohtori, Observation of Induced Shear Acoustic Phonons by Brillouin Scattering, Japanese Journal of Applied Physics **46**, 4626-4628 (2007).

[30] J. K. Krüger, B. Vincent, O. Elmazria, L. Bouvot, and P. Alnot, Brillouin microscopy on microwave-induced phonons in $LiNbO_3$, New Journal of Physics **6**, 57 (2004).

[31] M. Geilen, F. Kohl, B. Hillebrands, P. Pirro, A. Stefanescu, A. Müller, Interference of co-propagating Rayleigh and Sezawa waves observed with micro-focussed Brillouin Light Scattering Spectroscopy, arXiv: 2009. 04797. (2020).

[32] I. A. Privorotskii, Resonant transmission of electromagnetic energy through thick ferromagnetic films via phonons, IEEE Transactions on Magnetics **16**, 3 (1980).

[33] I. A. Privorotskii, R. A. B. Devine, and G. C. Alexandrakis, Generation and attenuation of phonons at ferromagnetic resonance in thick Ni films, Journal of Applied Physics **50**, 7732 (1979).

[34] C. Zhao, Y. Li, Z. Zhang, M. Vogel, J. E. Pearson, J. Wang, W. Zhang, V. Novosad, Q. Liu, A. Hoffmann, Phonon Transport Controlled by Ferromagnetic Resonance, Physical Review Applied **13**, 054032 (2020).

[35] R. Manenti, M. J. Peterer, A. Nersisyan, E. B. Magnusson, A. Patterson, and P. J. Leek, Surface

acoustic wave resonators in the quantum regime, Physical Review B **93**, 041411(R) (2016).

[36] B. A. Moores, L. R. Sletten, J. J. Viennot, and K. W. Lehnert, Cavity Quantum Acoustic Device in the Multimode Strong Coupling Regime, Physical Review Letters **120**, 227701 (2018).

[37] I. a. Feng, M. Tachiki, C. Krischer, and M. Levy, Mechanism for the interaction of surface waves with 200-Å nickel films, Journal of Applied Physics **53**, 177 (1982).

[38] D. Labanowski, V. P. Bhallamudi, Q. Guo, C. M. Purser, B. A. McCullian, P. C. Hammel, S. Salahuddin, Voltage-driven, local, and efficient excitation of nitrogen-vacancy centers in diamond Science Aavances **4**, eaat6574 (2018).

[39] R. Manenti, A. F. Kockum, A. Patterson, T. Behrle, J. Rahamim, G. Tancredi, F. Nori, and P. J. Leek, Circuit quantum acoustodynamics with surface acoustic waves, Nature Communications **8**, 975 (2017).